AD-A147 379 A LOOK-UP PERIMETER INTRUSION SENSOR: EVALUATION OF A CONTINUOUS ARRAY(U) ROME AIR DEVELOPMENT CENTER GRIFFISS AFB NY J L POIRIER ET AL. APR 84 1/1

UNCLASSIFIED RADC-TR-84-96 F/G 17/9 NL

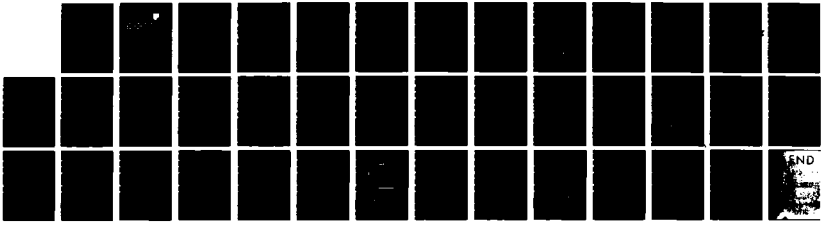

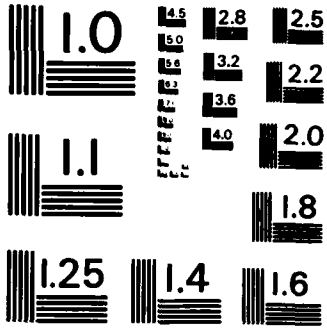

(12)

RADC-TR-84-96
In-House Report
April 1984

A LOOK-UP PERIMETER INTRUSION SENSOR: EVALUATION OF A CONTINUOUS ARRAY

J. Leon Poirier
Garret E. Murdza

ROME AIR DEVELOPMENT CENTER
Air Force Systems Command
Griffiss Air Force Base, NY 13441

This report has been reviewed by the RADC Public Affairs Office (PA) and is releasable to the National Technical Information Service (NTIS). At NTIS it will be releasable to the general public, including foreign nations.

RADC-TR-84-96 has been reviewed and is approved for publication.

APPROVED: Philipp Blacksmith

PHILIPP BLACKSMITH
Chief, EM Techniques Branch
Electromagnetic Sciences Division

APPROVED: Allan C. Schell

ALLAN C. SCHELL
Chief, Electromagnetic Sciences Division

FOR THE COMMANDER: John A. Ritz

JOHN A. RITZ
Acting Chief, Plans Office

If your address has changed or if you wish to be removed from the RADC mailing list, or if the addressee is no longer employed by your organization, please notify RADC (EECS) Hanscom AFB MA 01731. This will assist us in maintaining a current mailing list.

Do not return copies of this report unless contractual obligations or notices on a specific document requires that it be returned.

Unclassified

SECURITY CLASSIFICATION OF THIS PAGE (When Data Entered)

REPORT DOCUMENTATION PAGE		READ INSTRUCTIONS BEFORE COMPLETING FORM
1. REPORT NUMBER RADC-TR-84-96	2. GOVT ACCESSION NO. AD-A147379	3. RECIPIENT'S CATALOG NUMBER
4. TITLE (and Subtitle) A LOOK-UP PERIMETER INTRUSION SENSOR: EVALUATION OF A CONTINUOUS ARRAY		5. TYPE OF REPORT & PERIOD COVERED In-House 6. PERFORMING ORG. REPORT NUMBER
7. AUTHOR(s) J. Leon Poirier Garret E. Murdza		8. CONTRACT OR GRANT NUMBER(s) N/A
9. PERFORMING ORGANIZATION NAME AND ADDRESS Rome Air Development Center (EECS) Hanscom AFB Massachusetts 01731		10. PROGRAM ELEMENT, PROJECT, TASK AREA & WORK UNIT NUMBERS 62702F 46001507
11. CONTROLLING OFFICE NAME AND ADDRESS Rome Air Development Center (EECS) Hanscom AFB Massachusetts 01731		12. REPORT DATE April 1984 13. NUMBER OF PAGES 37
14. MONITORING AGENCY NAME & ADDRESS(if different from Controlling Office)		15. SECURITY CLASS. (of this report) Unclassified 15a. DECLASSIFICATION DOWNGRADING SCHEDULE

16. DISTRIBUTION STATEMENT (of this Report)

Approved for public release; distribution unlimited.

17. DISTRIBUTION STATEMENT (of the abstract entered in Block 20, if different from Report)

18. SUPPLEMENTARY NOTES

RADC Project Engineer: J. Leon Poirier/EECS

19. KEY WORDS (Continue on reverse side if necessary and identify by block number)

Intrusion sensor
Look-Up sensor

20. ABSTRACT (Continue on reverse side if necessary and identify by block number)

A look-up sensor to detect low altitude airborne intruders is proposed and analyzed. The sensor, which consists of a continuous array of radiators, produces a vertical detection zone around the perimeter of the protected installation. Expressions for its design and detection performance are developed and used to generate a set of parametric coverage diagrams for the sensor. A multistatic implementation of the system is examined that gives the unambiguous measurement of intruder range and altitude. Finally, control of the transmitter pulse shape to reduce the radiation pattern sidelobes is discussed.

DD FORM 1 JAN 73 1473

Unclassified

SECURITY CLASSIFICATION OF THIS PAGE (When Data Entered)

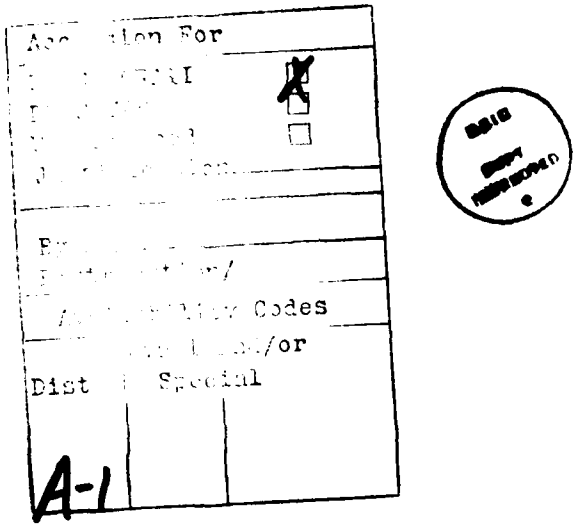

Contents

Illustrations

A Look-Up Perimeter Intrusion Sensor: Evaluation of a Continuous Array

1. INTRODUCTION

This report describes and analyzes a look-up sensor intended to encircle the perimeter of a large installation and detect low altitude airborne threats such as helicopters or hang gliders.

A number of intrusion sensors have been developed to detect intruders on the ground. Their operation has been based on several different physical phenomena including acoustic, seismic, optical, infrared, and radio waves.[1-3] Most of these have very limited detection zones or require the intruder to make physical contact with the sensor. In contrast, the detection fields of radar-like radio frequency systems can be made to extend significant distances from the sensor and can thus detect an intruder where conventional sensors can not.[4]

(Received for publication 18 April 1984)

1. GUIDAR Technical Brochure (1980) Computing Devices Co., Ottawa, Ontario, Canada.

2. SPIR Technical Brochure (1980) Computing Devices Co., Ottawa, Ontario, Canada, December 1980.

3. Poirier, J. L. (1980) Estimation of the Zone of Detection of the Single Wire Individual Resource Protection Sensor, RADC-TR-80-258, AD A094137.

4. Gehman, J. B. (1981) Area Intruder Track Study, RADC-TR-81-314, AD A110621.

A sketch of a conceptual look-up sensor is depicted in Figure 1 where the sensor is deployed around the perimeter of an installation. The detection zone extends upwards from the ground and an object penetrating this zone would be detected. However, the value of the sensor would be greatly enhanced if it could also determine the position of the intrusion along the perimeter. One way to accomplish this is to drive the sensor with a pulse, rather than a continuous wave. The pulse travels along the sensor and excites a section of the sensor proportional to the duration of the pulse, thus producing an upward pointing beam. The beam moves along the sensor and intercepts the target. Some of the energy reflected by the target is received by the sensor and propagates back to its input. The time Δt that elapses between the transmission of the pulse and the return of its reflection from the target is a measure of the total distance to the target. The elapsed time is related to the target's position by

$$\Delta t = 2\{(X/v) + (Y/c)\} \quad ,$$

where X is the distance along the sensor to the point of intrusion, Y is the altitude of the target, and v and c are the propagation velocities of the pulse along the sensor and in free space respectively.

The generic sensor configuration that will be analyzed consists of a continuous array of radiators, each coupled to a suitable transmission line. When the pulse propagates along the transmission line the group of elements spanned by the pulse forms an upward pointing beam that moves along the sensor at its propagation velocity.

The equations describing the electromagnetic properties of the array making up the sensor structure will be developed by applying phased array theory. However, since the targets can be in the near-field of the array and the amplitude coefficients of successive elements can be different, the equations that result are not as compact as the far-field approximations often associated with linear arrays. The derived sensor equations will then be used as the basis for calculating the radar performance of the system from which some preliminary designs can be developed. Finally, the effects of tapering the coupling to insure a constant detection sensitivity and the temporal shaping of the pulse to control the effective sidelobes of the beam pattern will be addressed.

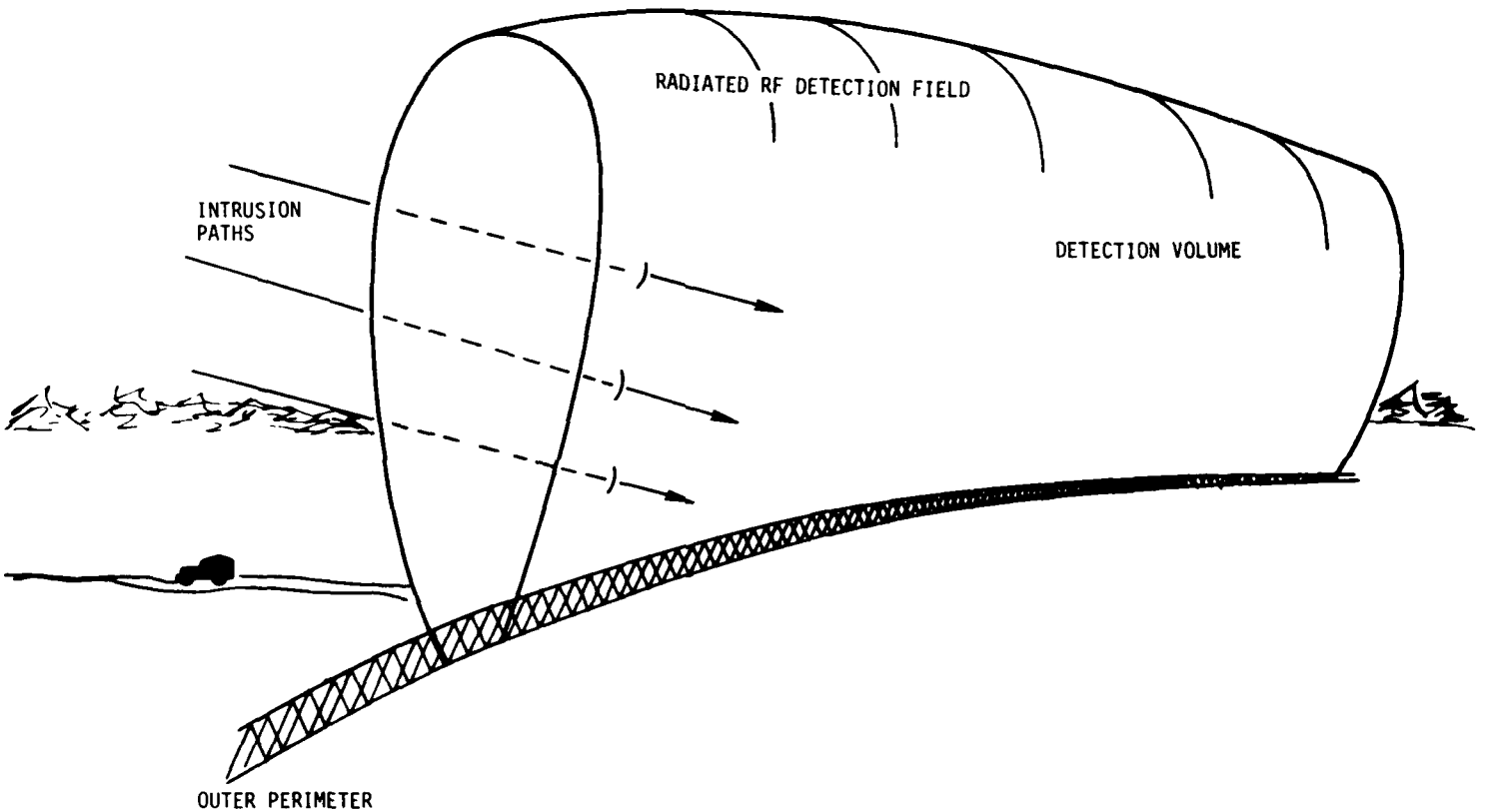

Figure 1. Artist's Concept of Look-Up Sensor

2. COMPUTATION OF SENSOR FIELDS

2.1 Dipole Fields

The θ component of electric field intensity due to a thin half-wavelength long dipole radiator oriented along the z axis (Figure 2) can be written as

$$\bar{E}_\theta = V_o \frac{e^{jkr}}{r} \frac{\cos[(\pi \cos\theta)/2]}{\sin\theta} \hat{\theta} \quad , \tag{1}$$

as long as the distance r from the center of the dipole to the field point exceeds a few wavelengths.[5] The free space wavenumber is $k = 2\pi/\lambda$, V_o is the complex amplitude, θ is the polar angle, and $\hat{\theta}$ is the unit vector.

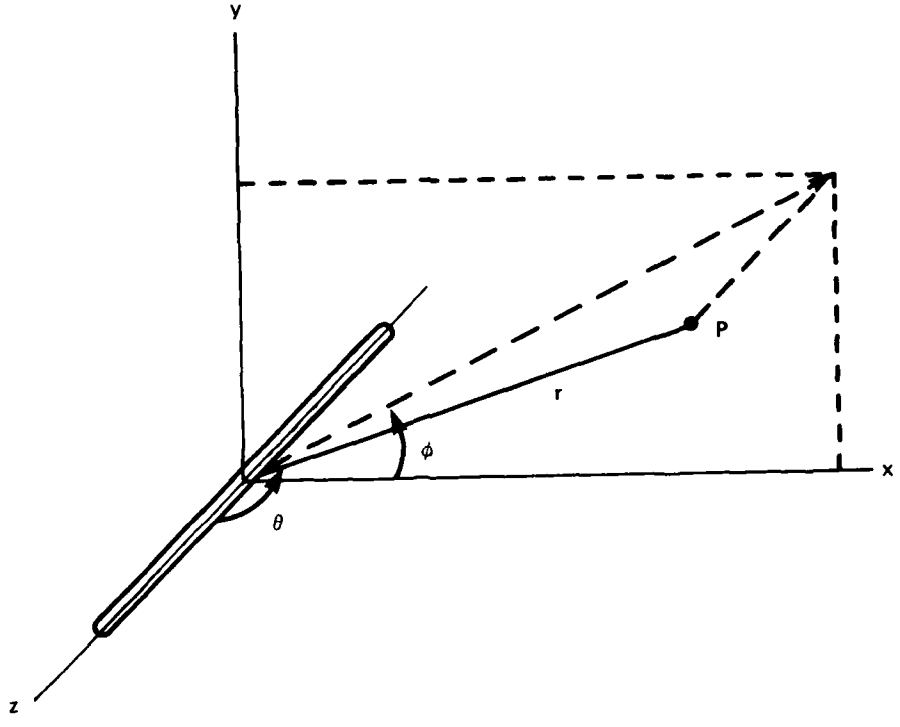

Figure 2. Dipole Element and Its Coordinate System

5. Jasik, H. (Ed.) (1961) Antenna Engineering Handbook, McGraw-Hill, N.Y.

The computations to follow may be further simplified if θ is set equal to $\pi/2$ thus restricting attention to the xy plane. In this case Eq. (1) becomes

$$\bar{E}_\theta = V_o \frac{e^{jkr}}{r} \hat{\theta} \tag{2}$$

where $\hat{\theta}$ is seen to be equal to $-\hat{z}$.

The array is made up of a number of similar dipoles arranged as indicated in Figure 3. The local field of each dipole is given by Eq. (2) in terms of the coordinates of that element. In contrast, the field quantities of the array will usually be given in terms of the coordinates of the first excited element or the center of the array. All dipoles are in the xz plane, lie parallel to the z axis, and are separated by a distance d. Each element is considered to be excited by a transmission line with propagation characteristics described by an attenuation factor α and a phase constant β. The length of line between elements is d', that between the input and the first element is x'_1, and that between the last element and the matched load terminating the line d'_L. Primed quantities refer to the transmission line lengths and unprimed quantities to the spatial locations of the

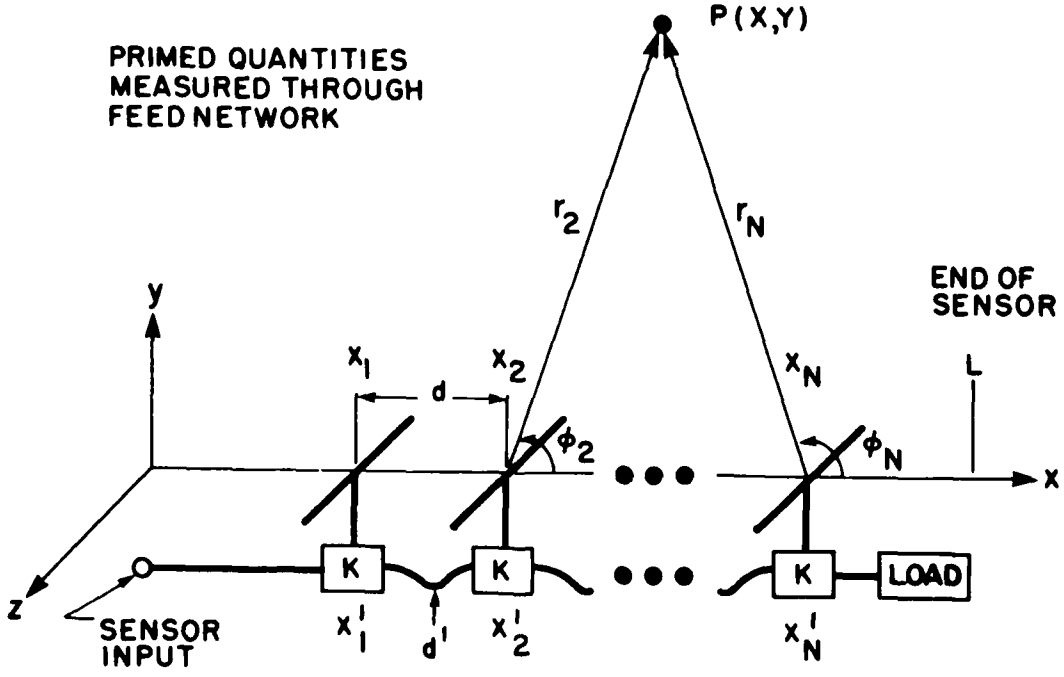

Figure 3. Sketch of Dipole Array

elements. The total length of the sensor is L and includes the length x_1. The degree of coupling (power) between the transmission line and the nth element is $|K_n|^2$.

The physical properties of the array need not be specified further at this time, since the sensor could be implemented in a number of ways. For example, the dipoles could be proximity-coupled to a long transmission line. Instead, the performance of the generic array shown in Figure 3 will be investigated.

2.2 Dipole Array

The total field at a point P(X, Y), due to the linear array of dipoles depicted in Figure 3, is the sum of the contributions from each of the elements. For N sources, this sum is

$$\bar{E}_\theta(X,Y) = \sum_{n=1}^{N} V_n \frac{e^{[-j(\omega t - kr_n)]}}{r_n} \hat{\theta} \quad , \tag{3}$$

where V_n is the complex amplitude of the nth element.

The power density is found from the average Poynting vector $\bar{P} = 1/2\ \mathrm{Re}(\bar{E} \times \bar{H}^*)$ to be

$$\bar{P} = \mathrm{Re} \sum_{n=1}^{N} \sum_{m=1}^{N} V_n V_m^* \frac{e^{[jk(r_n - r_m)]}}{2z_o r_n r_m} \hat{\theta} \times \hat{\phi}_m \quad , \tag{4}$$

where z_o is the intrinsic impedance of free space. The normalized field intensity $\bar{E}_{\theta N}$ and the normalized power density $\bar{P}_N$ are obtained by dividing $\bar{E}_\theta$ and $\bar{P}$ by the magnitude of their respective maximum values.

If the observation point is sufficiently far from the array, then Eqs. (3) and (4) can be specialized and some additional quantities defined. From Figure 3 it is seen that r_n in the numerator of Eq. (1) satisfies the relation $r_{n+1} = r_n - (x_{n+1} - x_n) \cos \phi$, that $r_1 = R$, and that r_n in the denominator can be replaced by R. These changes are valid for $R \geq 2[(N - 1)d]^2/\lambda$ where (N - 1)d is the length of the array. Dropping the vector notation and setting $(x_{n+1} - x_n) = d$, let us write Eq. (1) as

$$E_{\theta F} = e^{[-j(\omega t - kR)]} \sum_{n=1}^{N} V_n \frac{e^{[-j(n-1)kd \cos \phi]}}{R} \tag{5}$$

and the normalized far-field intensity $E_{\theta FN}$ as

$$E_{\theta FN} = e^{[-j(\omega t - kR)]} \sum_{n=1}^{N} V_n e^{[-j(n-1)kd \cos \phi]} \Bigg/ \sum_{n=1}^{N} V_n \quad . \tag{6}$$

The power density may be written as

$$P_F = E_{\theta F} E^*_{\theta F}/2z_o \tag{7}$$

and the normalized power density as

$$P_{FN} = E_{\theta FN} E^*_{\theta FN} \quad . \tag{8}$$

If $V_n = V$, then Eq. (8) reduces to the familiar expression for the far-field power pattern of a linear array of N isotropic elements (or dipole elements, as in this case, when the field is measured only in the xy plane).[6] That is,

$$P_{FN} = \frac{\sin^2[(Nkd \cos \phi)/2]}{N^2 \sin^2[(kd \cos \phi)/2]} \quad . \tag{9}$$

The normalized power patterns P_{FN} for several arrays with element spacing $d = \lambda/2$ and $V_n = V_o$ are shown in Figure 4. The maximum gain occurs at $\phi = 90^o$ (broadside) and, generally, the longer the array, the narrower the main beam and the lower the average sidelobe level.

The ultimate purpose of this analysis is to determine the radar detection performance of the sensor as a function of the target coordinates X and Y. Therefore, it is more appropriate to present the power pattern of the array as a function of the X coordinate of the target as it moves along the length of the sensor in the xy plane with the altitude Y taken as some arbitrary but fixed value. Placing the center of the array at $x_o = L/2$ yields

$$R = [(X - x_o)^2 + Y^2]^{1/2} \tag{10}$$

---

6. Krauss, J.D. (1950) Antennas, McGraw-Hill, N.Y.

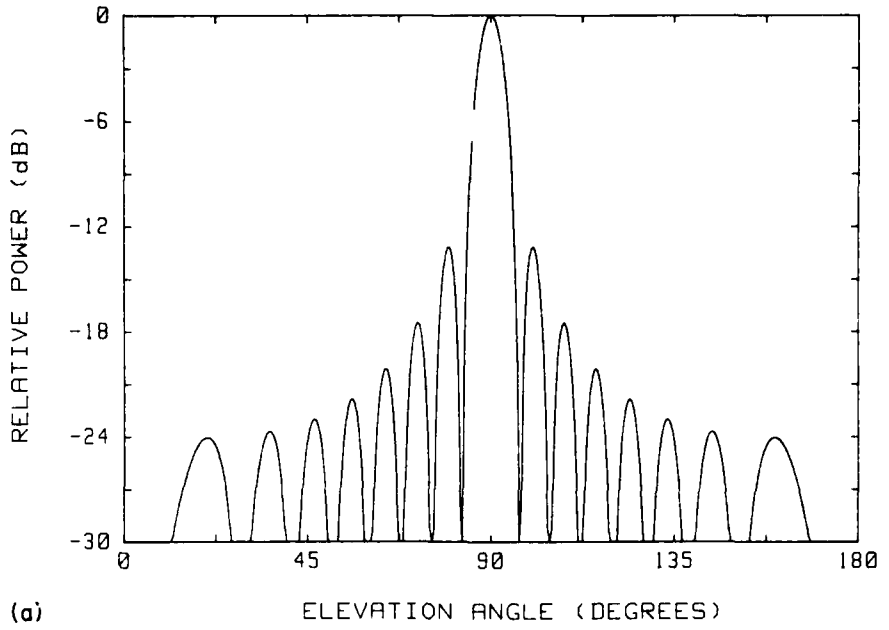

(a)

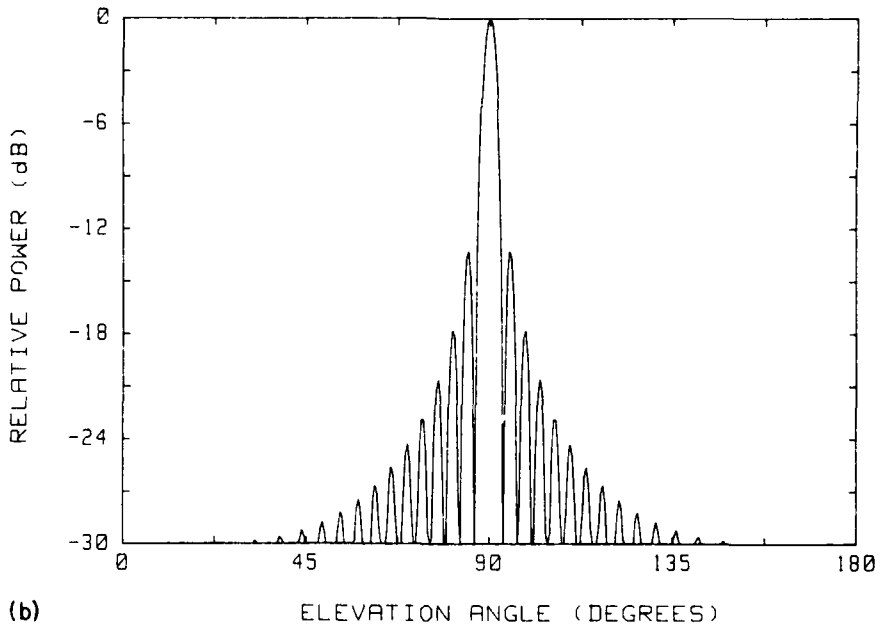

(b)

Figure 4. Normalized Far-Field Power Patterns for Several Arrays. $d = \lambda/2$. (a) N = 16, (b) N = 32, and (c) N = 64

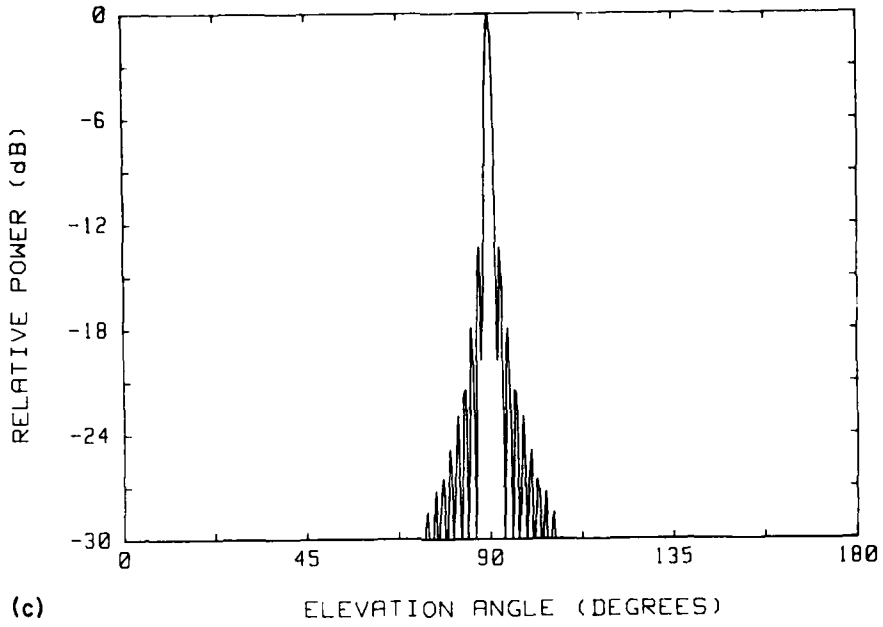

(c)

Figure 4. Normalized Far-Field Power Patterns for Several Arrays. $d = \lambda/2$. (a) N = 16, (b) N = 32, and (c) N = 64 (Contd)

and

$$\phi = \tan^{-1}[Y/(X - x_o)] \quad . \tag{11}$$

The expression for the normalized far-field intensity obtained by inserting Eqs. (10) and (11) into Eq. (5) and then normalizing to the magnitude of the maximum field intensity at $X = x_o$ is

$$E_{\theta FN} = Y\, e^{\left(-j\left\{\omega t - k[(X-x_o)^2 + Y^2]^{1/2}\right\}\right)} \frac{\sum_{n=1}^{N} V_n\, e^{\left(-j(n-1)kd\cos\{\tan^{-1}[Y/(X-x_o)]\}\right)}}{[(X-x_o)^2 + Y^2]^{1/2} \sum_{n=1}^{N} V_n} \quad . \tag{12}$$

$E_{\theta FN}$ depends on R as well as ϕ since R now is also a function of ϕ. P_{FN}, obtained by multiplying $E_{\theta FN}$ in Eq. (12) by its complex conjugate, is plotted in Figure 5 for a 32-element array centered on a 1-km line and shows the relative power density that would be incident on a target moving in the X direction at a constant altitude $Y = 2(N - 1)^2 d^2/\lambda$.

In practice, the target would often not be at a height $Y \geq 2(N - 1)^2 d^2/\lambda$, the far-field distance for the array, and Eq. (4) would have to be evaluated formally to obtain P. Figure 3 shows that $\hat{\theta} = -\hat{z}$ and $\hat{\phi} = -\sin\phi\,\hat{x} + \cos\phi\,\hat{y}$. Thus

$$\overline{E}_\theta = -\sum_{n=1}^{N} V_n \frac{e^{[-j(\omega t - kr_n)]}}{r_n}\,\hat{z} \quad , \tag{13}$$

$$\overline{H}_\phi^* = \sum_{m=1}^{N} V_m^* \frac{e^{[j(\omega t - kr_m)]}}{z_o r_m}\,(-\sin\phi_m\hat{x} + \cos\phi_m\hat{y}) \quad , \tag{14}$$

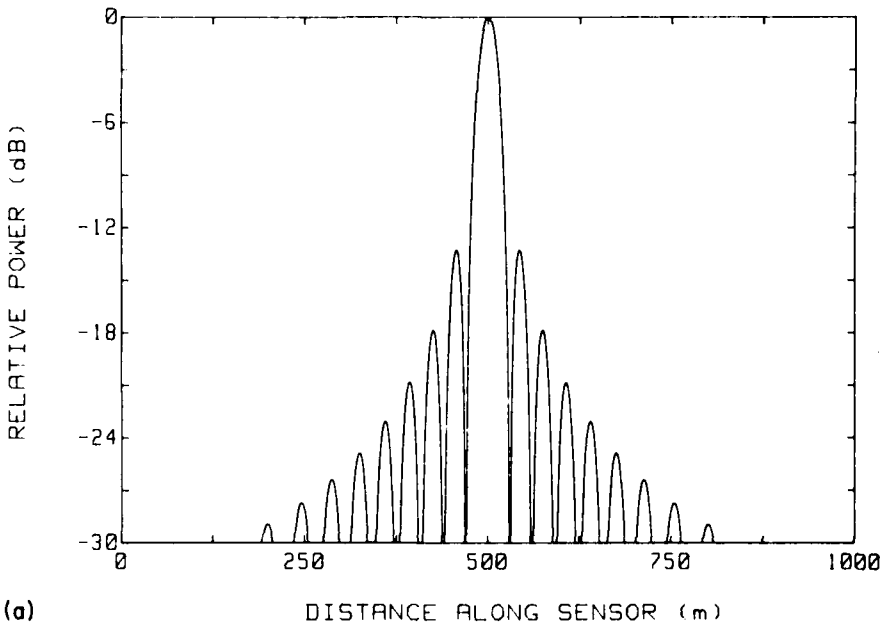

(a)

Figure 5. Normalized Far-Field Power Density at a Constant Height Above Sensor. L = 1 km, $x_o = L/2$, $d = \lambda/2$, $\lambda = 1$ m, $V_n = V$, and $Y = 2(N - 1)^2 d^2/\lambda$. (a) N = 32 and (b) N = 64

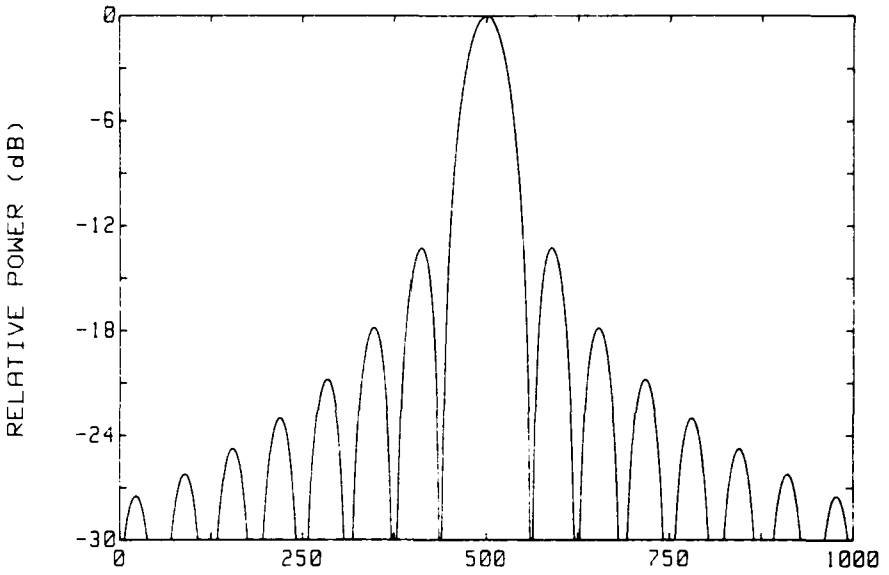

(b)

Figure 5. Normalized Far-Field Power Density at a Constant Height Above Sensor. L = 1 km, $x_o = L/2$, $d = \lambda/2$, $\lambda = 1$ m, $V_n = V$, and $Y = 2(N - 1)^2 d^2/\lambda$. (a) N = 32 and (b) N = 64 (Contd)

and

$$\overline{P} = \frac{\mathrm{Re}\,(\overline{E}_\theta \times \overline{H}_\phi^*)}{2} \quad . \tag{15}$$

When Y is sufficiently large, Eq. (15) reduces to the expression given by Eq. (7) since then, $\phi_m = \phi$ for all m.

For a constant height target, $r_m = [(X - x_m)^2 + Y^2]^{1/2}$, $\phi_m = \tan^{-1}[Y/(X - x_m)]$, $x_m = x_1 + (m - 1)d$, and $x_1 = \{L - (N - 1)d\}/2$, where L is the total length of the sensor. Similar expressions apply for the index n. With these substitutions, the power density expressed by Eq. (15), normalized to its value broadside to the array, is plotted in Figure 6 for three values of Y to show the effect of the target's close proximity to the array elements. Comparison of the patterns shows a filling of the near-in nulls when the target is not in the far-field of the array. This is as expected because of the quadratic phase error and the increasing amplitude error. The apparent narrowing of the main beam results from the fact that for a target near the ground, the angle ϕ changes very rapidly with X compared to a higher target. Thus the effective linear resolution of such a system will be a function of the height of the target as well

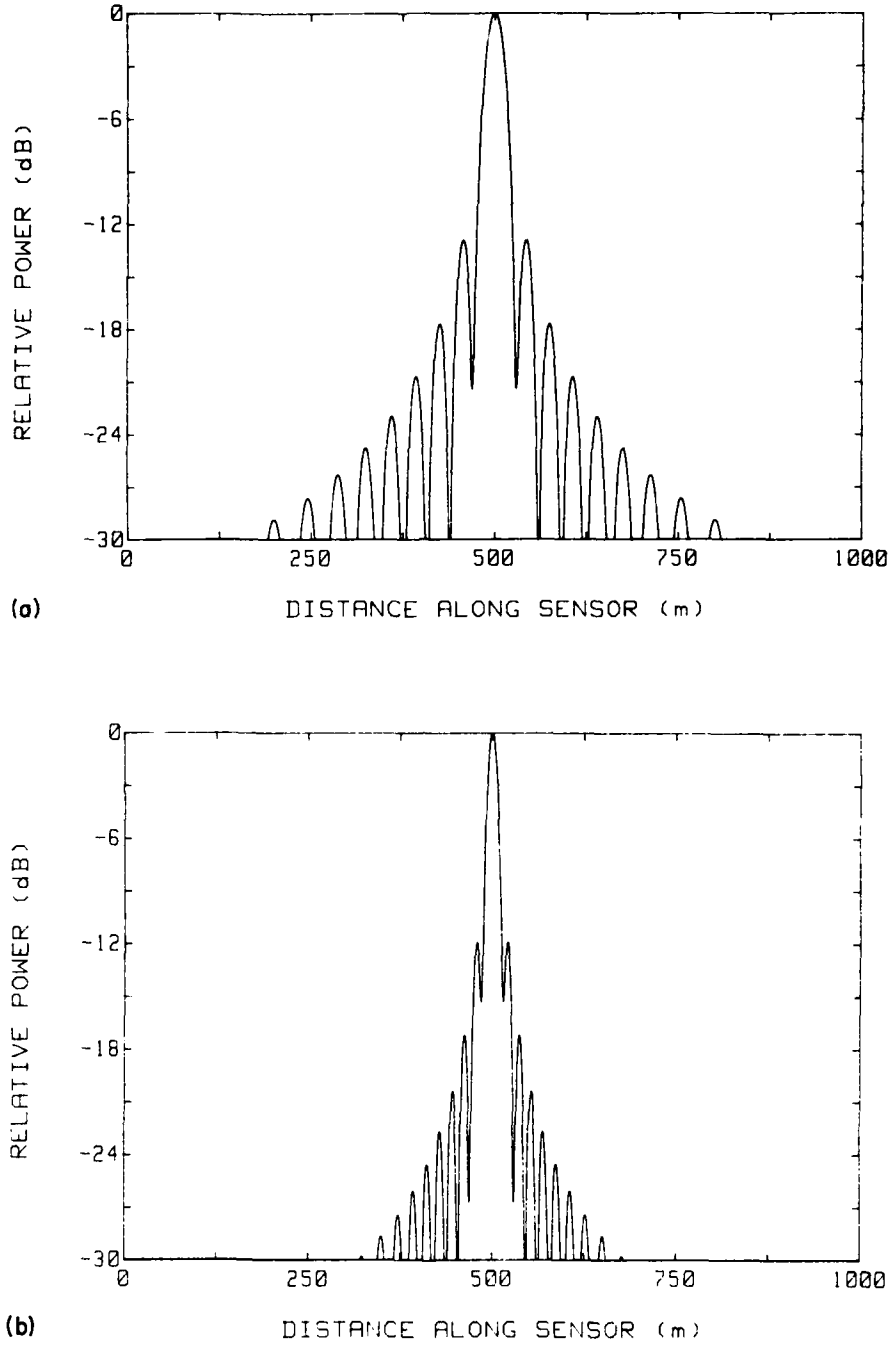

Figure 6. Normalized Near-Field Power Density at a Constant Height Above Sensor. L = 1 km, x_o = L/2, N = 32, d = $\lambda/2$, λ = 1 m, and V_n = V. (a) Y = 2 $(N - 1)^2 d^2/\lambda$, (b) Y = $(N - 1)^2 d^2/\lambda$, and (c) Y = $0.2(N - 1)^2 d^2/\lambda$

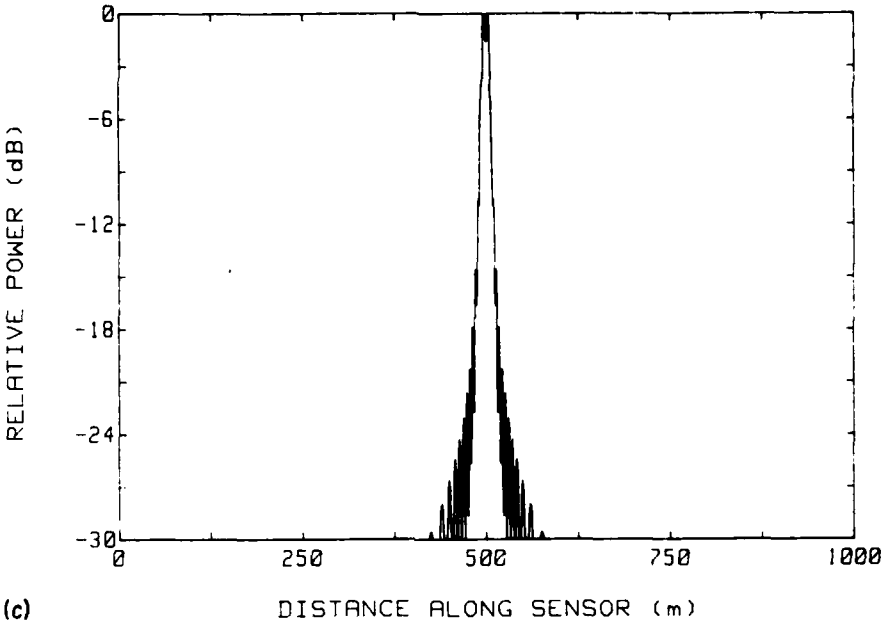

(c)

Figure 6. Normalized Near-Field Power Density at a Constant Height Above Sensor. L = 1 km, x_o = L/2, N = 32, d = $\lambda/2$, λ = 1 m, and V_n = V. (a) Y = 2 $(N-1)^2d^2/\lambda$, (b) Y = $(N-1)^2d^2/\lambda$, and (c) Y = 0.2$(N-1)^2d^2/\lambda$ (Contd)

as the length of the array. The pattern in Figure 6(a) should be compared with that in Figure 5(a) to show that Eqs. (15) and (7) produce progressively closer results as R, the distance from the center of the array to P, increases.

2.3 Element Excitation

The field distribution expressed by Eq. (3) should be modified to account for the phase and amplitude of the signal exciting successive elements of the array. This can be done by letting V_n take the form

$$V_n = V_o\, e^{(-\alpha + j\beta)[x_1' + (n-1)d']}\, K(1-|K|^2)^{[(n-1)/2]} \quad , \tag{16}$$

where V_o is the transmission line input voltage, α and β its propagation constants, and K the element coupling coefficient. With these changes, Eq. (3) can be written as

$$\bar{E}_\theta = V_o \, e^{[(-\alpha+j\beta)x_1' - j\omega t]}$$

$$\hat{\theta} \sum_{n=1}^{N} \frac{e^{[(-\alpha+j\beta)(n-1)d' + jkr_n]} \, K(1-|K|^2)^{(n-1)/2}}{r_n} \tag{17}$$

and the power density found with Eq. (15). The expression for the far-field intensity corresponding to Eq. (17) is

$$E_{\theta F} = V_o \, e^{[(-\alpha+j\beta)x_1' - j(\omega t - kR)]} \sum_{n=1}^{N} \frac{e^{\{[(-\alpha+j\beta)d' - jkd \cos \phi](n-1)\}}}{R}$$

$$K(1-|K|^2)^{(n-1)/2} \quad . \tag{18}$$

From the preceding discussion it can be seen that the power radiated from successive elements decreases steadily because of the attenuation of the transmission line and the energy coupled to the previous elements. To provide equal power radiated from each element, the coefficients must be varied along the array. The new coefficients K_n that will ensure that equal power is coupled to each element are computed as follows.

The power reaching the position of the nth element along the transmission line can be expressed as

$$P_n = V_o V_o^* \, e^{\{-2\alpha[x_1' + (n-1)d']\}} \prod_{q=1}^{n-1} \frac{(1-K_q K_q^*)}{2Z_o} \tag{19}$$

for $n > 1$, where Z_o is the input impedance of the transmission line. The product $P_n K_n K_n^*$ thus is equal to the power radiated from the nth element and $P_n(1 - K_n K_n^*)$ is the power available to continue down the line to excite the remainder of the elements. The requirement for an equal amplitude signal to be radiated from each element then gives the recursion formula $P_n K_n K_n^* = P_{n+1} K_{n+1} K_{n+1}^*$ from which an expression can be constructed that gives the value of the coupling coefficient for any element in terms of the first. The result is

$$K_n K_n^* = \frac{K_1 K_1^*}{e^{[-2(n-1)\alpha d']} - K_1 K_1^* \sum_{q=1}^{n-1} e^{[-2q\alpha d']}} \tag{20}$$

for $n > 1$. The power remaining immediately after the last element ($n = N$) is $P_L = P_N(1 - K_N K_N^*)$ and is absorbed by the load terminating the feeding cable. Successive application of Eq. (19) under the restriction of Eq. (20) yields

$$P_L = P_T e^{[-2\alpha x_1']} \left(e^{[-2\alpha(N-1)d']} - K_1 K_1^* \sum_{q=0}^{N-1} e^{-2\alpha q d'} \right) , \tag{21}$$

where $P_T = V_o V_o^* / 2Z_o$, the input power. Equation (21) is solved for $K_1 K_1^*$ and substituted into Eq. (20) to obtain the remaining K_n. The results are plotted in Figure 7 for several values of the parameter $A = P_L/P_T$.

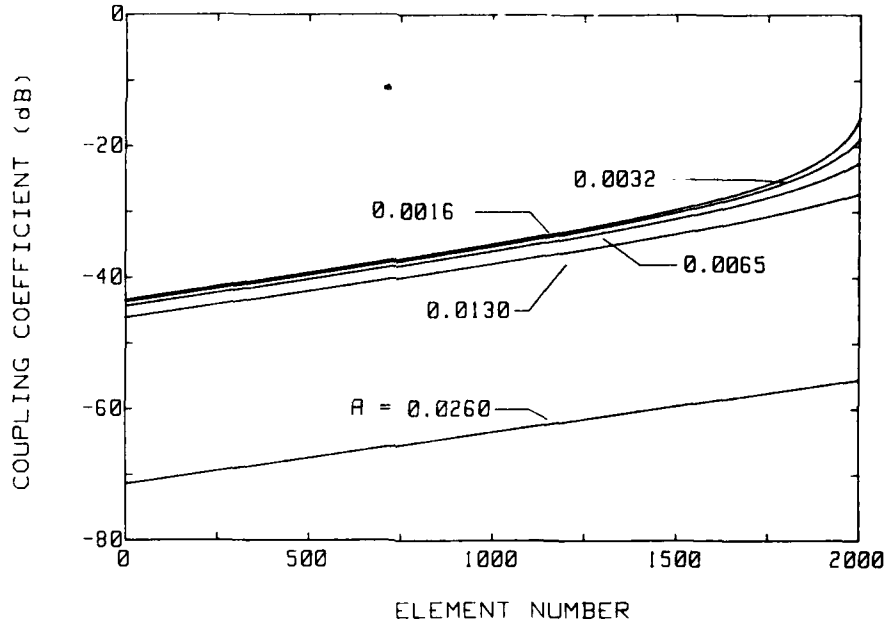

Figure 7. Element Coupling Coefficients for Uniform Element Excitation. $d' = 0.73$ m, $\lambda = 1$ m, $N = 2000$, and $\alpha = 0.0025$ Neper/m

2.4 Pulse Illumination

When a pulse propagates down the transmission line, a certain time must elapse before the energy reaches points farther down the line. Thus, each element of the array is energized at a slightly later time than the previous element and during this transient interval the beam forming properties of the array are incomplete.

To analyze this behavior it is assumed that the transmission line and the radiating elements are not dispersive so that each frequency component of the pulse is similarly affected. To account for the propagation time along the transmission line, Eq. (16) is written as

$$V_n(x_n', t) = f\left(t - \frac{x_n'}{v}\right) V_o K_n \, e^{[(-\alpha+j\beta)(x_1' + (n-1)d')]} \prod_{p=1}^{n-1} (1-|K_p|^2)^{1/2} \quad , \qquad (22)$$

where

$$f(t - x_n'/v) = 1 \text{ for } 0 < t - x_n'/v \leq \tau$$

$$= 0 \text{ otherwise.}$$

Thus a pulse does not arrive at the point x' on the transmission line for x'/v sec after it is applied to the input and persists for only τ sec, the pulse width, after which time the voltage remains zero until the arrival of another pulse. The excitation of each element of the array occurs d'/v sec after the previous element and the energy radiated by each element reaches the field point P(X, Y) r_n/c sec after that. To account for this, Eq. (17) is written as

$$\bar{E}_\theta = V_o \, e^{[(-\alpha+j\beta)x_1' - j\omega t]}$$

$$\sum_{n=1}^{N} K_n \, f\left[t - \left(\frac{x_n'}{v}\right) - \left(\frac{r_n}{c}\right)\right] \, e^{[(-\alpha+j\beta)(n-1)d' + jkr_n]}$$

$$\prod_{p=1}^{n-1} (1-|K_p|^2)^{1/2} \, \frac{\hat{\theta}}{r_n} \quad , \qquad (23)$$

where

$$f[t - (x_n'/v) - (r_n/c)] = 1 \text{ for } 0 \le t - (x_n'/v) - (r_n/c) \le \tau$$
$$= 0 \text{ otherwise.}$$

In the limit as $\tau \to \infty$, $f[t - (x_n'/n) - (r_n/c)] \to 1$ and Eq. (23) reduces to the expression for E_θ given by Eq. (17). In a similar manner, the far-field intensity is represented as

$$E_{\theta F} = V_o \, e^{[(-\alpha+j\beta)x_1' - j(\omega t - kR)]}$$

$$\sum_{n=1}^{N} K_n \, f\left(t - \frac{x_n'}{v} - \frac{r_n}{c}\right) \, e^{\{[(-\alpha+j\beta)d' - jkd\cos\phi](n-1)\}}$$

$$\prod_{p=1}^{n-1} \frac{(1-|K_p|^2)^{1/2}}{R} \quad . \tag{24}$$

The last two equations can be written in much simpler form if the constraint that equal power be radiated from each element is enforced. Then the coupling coefficients of each element increase to compensate exactly for radiation and line loss and Eqs. (23) and (24) can be written as

$$\bar{E}_\theta = V_o \, K_1 \, e^{[(-\alpha+j\beta)x_1' - j\omega t]}$$

$$\sum_{n=1}^{N} f\left(t - \frac{x_n'}{v} - \frac{r_n}{c}\right) e^{[j\beta d'(n-1) + jkr_n]} \, \frac{\hat{\theta}}{r_n} \tag{25}$$

and

$$E_{\theta F} = V_o \, e^{[(-\alpha+j\beta)x_1' - j(\omega t - kR)]}$$

$$\sum_{n=1}^{N} K_1 \, f\left(t - \frac{x_n'}{v} - \frac{r_n}{c}\right) \, \frac{e^{j(\beta d' - kd\cos\phi)(n-1)}}{R} \quad . \tag{26}$$

Inspection of Eq. (23) shows that not all N elements of the array may be excited simultaneously. For example, when $v\tau < (N-1)d'$, the span of the pulse is less than the length of the array and the coefficients $f[t - (x'_n/v) - (r_n/c)]$ will be identically zero for some of the elements and the maximum gain of the array will not be realized. Only when $v\tau \geq (N-1)d'$ will all elements be illuminated at the same time for at least part of the pulse duration period. When the array is incompletely illuminated, the maximum number of excited elements is $N' = v\tau/d' + 1$.

The peak value of $P_F = (\text{Re } \bar{E}_{\theta F} \times \bar{H}^*_{\phi F})/2$ normalized to the full array value is plotted in Figure 8 to show the effect of the transient phenomenon on the power density. Inspection of the curves shows that until the pulse spans the entire array the beam is incompletely formed and the power density at P(X, Y) is below its maximum possible value. With the fill time $F = (N-1)d'/v$ and $\tau = 0.5F$, only half the array elements are excited and the greatest gain reached is 6 dB below the full array gain. For $\tau = F$, the full gain is obtained only for the instant that the pulse remains centered on the array and every element is excited. For $\tau > F$, the gain remains at its maximum value for proportionally longer intervals.

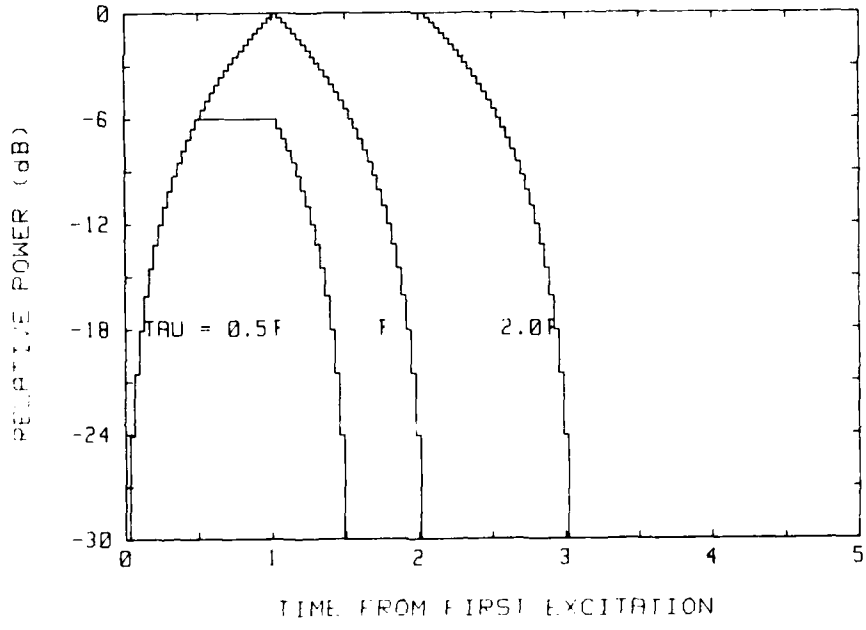

Figure 8. Power Density for an Incompletely Excited Array. N = 32, L = 1000 m, λ = 1 m, v = 0.73c, d' = 0.73 m, d = $\lambda/2$, and F = (N - 1)d'/v

2.5 Continuous Array

When the number of elements on the transmission line is large enough so that $v\tau < (N-1)d'$, the array is continuous and the width of the pulse on the line determines the length of the excited segment. As the pulse travels down the transmission line, the position of this subarray also moves along with the pulse. Thus a beam is formed that also moves down the line at a velocity equal to the propagation velocity of the line. The power density at a point above the sensor is a time-dependent function that grows to a maximum value as the traveling beam intercepts it and then decays to zero gradually after it has passed.

The power density produced by a pulse traveling down the continuous array can be obtained from Eqs. (25) and (26) by summing over every element of the sensor instead of the few that made up the finite array. To demonstrate the effect of this, the power density at a point halfway down a 1-km long sensor populated with dipoles along its entire length is plotted in Figure 9 as a function of time for several field point heights. The abscissa in Figure 9 begins at:

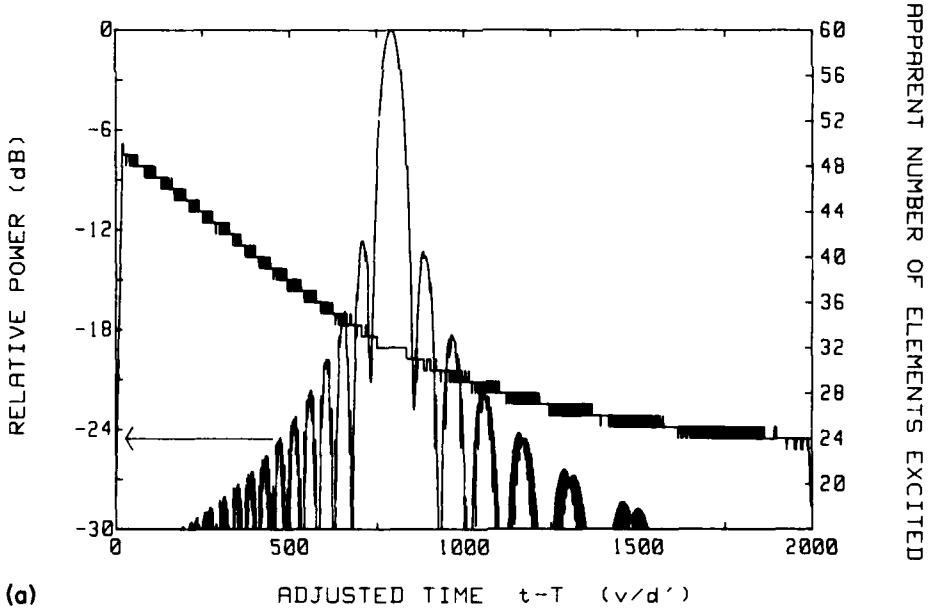

Figure 9. Power Density for Continuous Array. $\tau = 10.333 \times 10^{-8}$ sec, L = 1000 m, λ = 1 m, v = 0.73c, d' = 0.73 m, d = $\lambda/2$, $x_1' = 0$, N' = 32, X = L/2, and $T = [x_1' + (N' - 1)d'/2]/v + [Y^2 + (X - (N' - 1)d/2)^2]^{1/2}/c$. (a) $Y = 2(v\tau)^2/\lambda$, (b) $Y = (v\tau)^2/\lambda$, and (c) $Y = 20(v\tau)^2/\lambda$

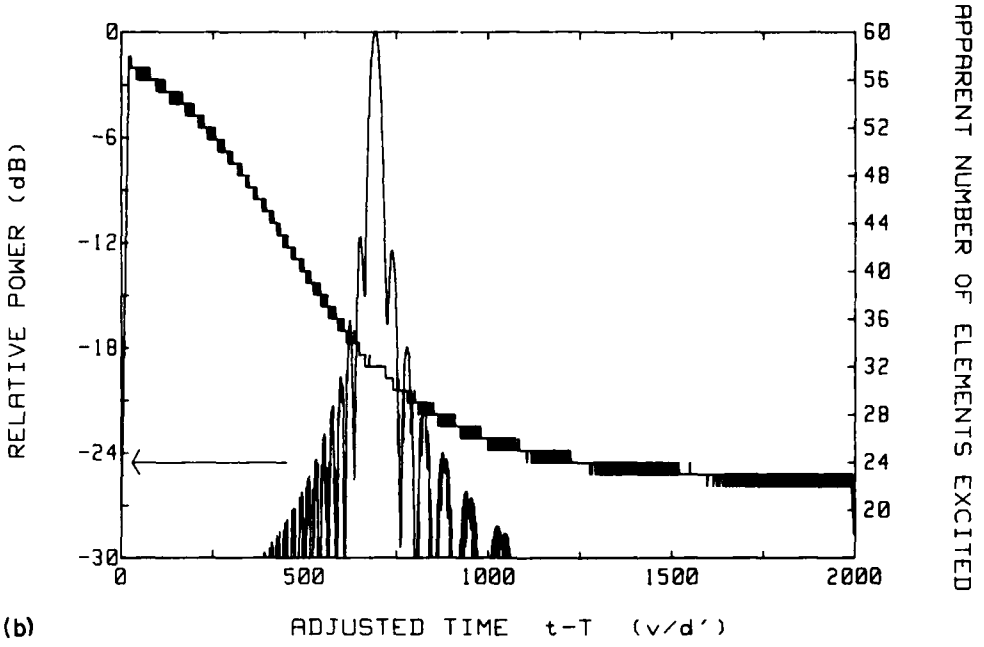

(b)

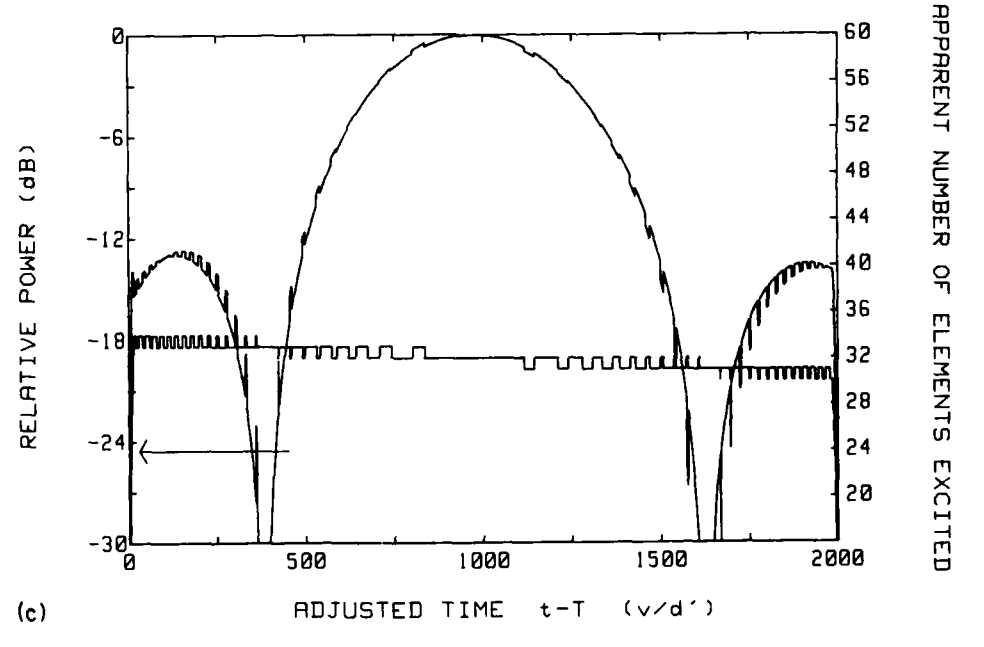

(c)

Figure 9. Power Density for Continuous Array. $\tau = 10.333 \times 10^{-8}$ sec, L = 1000 m, λ = 1 m, v = 0.73c, d' = 0.73 m, d = $\lambda/2$, $x_1' = 0$, N' = 32, X = L/2, and $T = [x_1' + (N' - 1)d'/2]/v + [Y^2 + (X - (N' - 1)d/2)^2]^{1/2}/c$. (a) $Y = 2(v\tau)^2/\lambda$, (b) $Y = (v\tau)^2/\lambda$, and (c) $Y = 20(v\tau)^2/\lambda$ (Contd)

$$T = \frac{[x_1' + (N'-1)d'/2]}{v} + \frac{[Y^2 + (X - (N'-1)d/2)^2]^{1/2}}{c} \quad ;$$

the time required for the center of the excited subarray of N' elements to reach the first element and the signal transmitted from the leading element to have reached P(X, Y). The buildup and decay of the density traces out the subarray's radiation pattern. However, it is apparent that although the curve has many of the properties of the patterns shown in Figure 6, its sidelobe structure is markedly different. The sidelobe spacing during the buildup phase is smaller than that during the decay phase of the pattern. This is easily explained and is a result of the high propagation velocity of the subarray along the sensor. It might be expected that the contributions at P(X, Y) from successive elements would arrive at time intervals of d'/v. However, the spatial path lengths from successive elements become progressively shorter up to the element immediately under the field point, after which they become progressively longer. Thus during buildup, contributions from successive elements reach the field point P(X, Y) at intervals shorter than d'/v. As a result, the elements appear to be more closely spaced, the sidelobe spacing decreases, and the sidelobe decay rate increases. When the subarray is in the neighborhood of the target location X, this effect has disappeared because the spatial pathlengths from successive elements to the target are nearly equal. In this region the pattern structure and subarray gain correspond to an array of $N' = v\tau/d' + 1$ elements. Beyond this region, the arrival times of successive contributions are delayed because the spatial pathlengths are progressively longer. The result is that the subarray appears to have fewer, more widely spaced elements. Its pattern then shows greater spacing between sidelobes and a slower decay rate than during the buildup phase.

The number of elements excited at any one time is always the same (once the entire pulse is on the sensor) and equal to $N' = v\tau/d' + 1$. However, as discussed above, the apparent number of elements observed at P(X, Y) varies as the subarray propagates across the sensor. The apparent number of subarray elements M is equal to the number of element locations x_n for which

$$0 \leq t - (x_n'/v) - (r_n/c) \leq \tau \quad . \tag{27}$$

The value of M so determined is plotted on the right in Figure 9 for each of the curves. The staircase character of the curve is a result of the integer counting that results from applying Eq. (27). The count can vary by one element for the same interval depending on the relative placement of the count window. It is this

variation in M that produces the noisy structure in the sidelobe region of the pattern. Notice that at the peak of the beam $M = N' = (v\tau/d') + 1 = 32$ as expected.

The effect of height Y above the sensor on the power density is apparent from the comparison of Figures 9(a), 9(b), and 9(c), which should also be compared with the corresponding curves of Figure 6. The structure of these curves would have been observed at P(X, Y) if that array had been moved slowly along the ground over the distance occupied by the sensor.

An estimate of the apparent number M of radiators excited, as a function of time, can be obtained from the relation

$$M = \{\tau/(dt/dr_n)\} + 1 \quad , \tag{28}$$

whenever $N >> N'$. The expression for dt/dr_n is

$$\frac{dt}{dr_n} = \frac{d'}{v} - \frac{(d/c)[X - (n-1)d]}{\{Y^2 + [X - (n-1)d]^2\}^{1/2}} \quad . \tag{29}$$

For $X = L/2$ and N odd, dt/dr_n at $n = 1$, $n = (N + 1)/2$, and $n = N$ is respectively

$$\frac{dt}{dr_1} = \frac{d'}{v} - \frac{(d/c)(L/2)}{[Y^2 + (L^2/4)]^{1/2}} \quad ,$$

$$dt/dr_{(N+1)/2} = d'/v \quad , \tag{30}$$

and

$$\frac{dt}{dr_N} = \frac{d'}{v} + \frac{(d/c)(L/2)}{[Y^2 + (L^2/4)]^{1/2}} \quad .$$

For reasonable values of L and Y, the effect of $v << c$ is to make the second term in Eq. (30) negligible so that $dt/dr_n = d'/v$ for all n. This corresponds to moving a physical subarray of N' elements slowly along the sensor while recording the power density at P. To show this, Eq. (28) is plotted in Figure 10 for several values of v.

In radar calculations, it is the maximum value of power density that determines detection performance. Thus only the peak value of the main beam need be computed to find the gain of the subarray. This occurs when the subarray is centered under the target, $M = N'$.

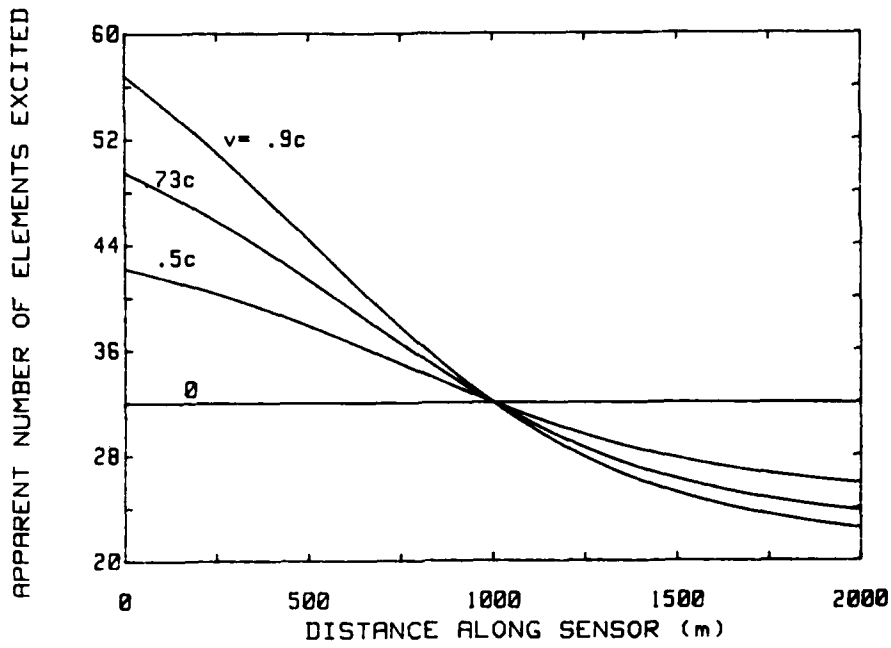

Figure 10. Apparent Number of Elements Excited, L = 1000 m, λ = 1 m, d' = 0.73 m, d = $\lambda/2$, and Y = $2(N' - 1)^2 d^2/\lambda$

An expression for the gain of the array sensor in the plane $\theta = \pi/2$ can be obtained from Eqs. (25) and (26) by setting $f[t - (x_n'/v) - (r_n/c)] = 1$. By definition, the gain $G(\theta,\phi) = 4\pi R^2 P(\theta,\phi)/P_o$, where P_o is the same input power that established the power density $P(\theta,\phi)$ and R the distance from the center of the array to the field point P(X, Y). Setting $P_o = V_o V_o^*/2Z_o$ and $\phi = \pi/2$, we obtain

$$G\left(\frac{\pi}{2},\frac{\pi}{2}\right) = 4\pi Y^2 K_1 K_1^* e^{-2\alpha x_1'} \sum_{q=1}^{N'} \sum_{p=1}^{N'} \cos[\beta d'(q-p) + k(r_q - r_p)] \frac{|\hat{\theta} \times \hat{\phi}_p|}{r_q r_p} \tag{31a}$$

and

$$G_F\left(\frac{\pi}{2},\frac{\pi}{2}\right) = 4\pi K_1 K_1^* e^{-2\alpha x_1'} \sum_{q=1}^{N'} \sum_{p=1}^{N'} \cos[(\beta d')(q-p)] \quad , \tag{31b}$$

where $r_p = [Y^2 + (X - d\{[(N'+1)/2] - p\})^2]^{1/2}$ and
$\phi_p = \tan^{-1}[Y/(X - d\{[(N'+1)/2] - p\})]$ with a similar expression for the index q. The maximum value of the far-field gain is $G_{FM} = 4\pi K_1 K_1^* N'^2 \exp[-2\alpha x_1']$ for $\beta d' = 2\pi$. By reciprocity, the sensor gain on receive is the same as on transmit.

3. RADAR PERFORMANCE ANALYSIS

3.1 Computation of Received Radar Signal

In this section, the performance of an array of dipoles used as a radar sensor will be analyzed. The system consists of a continuous array of dipoles along a perimeter of length L.

The power appearing at the terminals of the transmission line due to a reflection from a target at P(X, Y) is computed from the radar range equation in the form[7]

$$P_{REC} = \{P_o G_T/4\pi R^2\}\ \{\sigma/4\pi R^2\}\ \{\lambda^2 G_R/4\pi\} \quad , \tag{32}$$

where P_o is the input power; G_T and G_R the transmit and receive antenna gains respectively; λ the wavelength; and σ the radar cross-section, assumed here to be isotropic. The factors in the first bracket give the power density at the target produced by an antenna of gain G_T and input power P_o. The second bracket, when multiplied by the first gives the power density at the receiving antenna produced by a reflection from a target of radar cross section σ square meters. The factors in the last bracket represent the effective area A of the array that is related to its gain by the expression $G_R = 4\pi A/\lambda^2$.

Thus, Eq. (32) may be used to compute the power received at the input of the system from the interaction of the transmitted signals with a target entering the detection zone of the sensor. The performance of the sensor system depends on the magnitude of P_{REC} relative to the system noise as will be discussed in the next section.

3.2 Probability of Detection

The quantity that defines the performance of any radar is the signal-to-noise ratio S/N at its detector. For this analysis $S = P_{REC}$ and the noise is $N = kT_sB$, where k is the Boltzmann constant, T_s the system noise temperature in ^oK, and B the noise bandwidth. The receiver noise at the detector input is Rayleigh

7. Skolnik, M.I. (1962) Introduction to Radar Systems, McGraw-Hill, N.Y.

distributed and the received signal statistics depend on the size and shape of the target, its velocity, the operating frequency, and the pulse repetition frequency. In the present case, the received radar signal will be assumed to be nonfluctuating, a reasonable assumption for target sizes on the order of a wavelength.

In addition to the internally generated and galactic antenna noise, most radar receivers must also contend with clutter signals from the ground or other sources within the same range-azimuth cell as the target. A variety of techniques have been developed to separate the desired Doppler shifted signal that has been reflected by the moving target from the unshifted signal reflected from stationary clutter sources. As a result, the clutter power is reduced to the system noise level and often need not be considered.

The signals that finally reach the detector are the receiver noise and the target signals, the clutter signal having been eliminated by appropriate filters. The probability of detection P_D and the probability of false alarm F_A depend on the threshold at which the detector is set, the S/N ratio, and the statistics of the target signal. The P_D that can be expected for an assumed F_A can be calculated using well-known methods or can be obtained from curves that have been prepared for a large range of system parameters and fluctuation statistics.[8] For convenience, a few curves appropriate for the detection of a nonfluctuating target against Rayleigh noise are shown in Figure 11.

3.3 Performance Calculations

At this point it is necessary to select a set of system parameters upon which to base the performance calculations. The pulse repetition frequency (prf) was selected to achieve an unambiguous detection of a target at 1-km altitude along a 1 km long sensor. Thus $\text{prf} \leq 1/[(2Ld'/dv) + (2Y/c)] \leq 50$ kHz. The pulse width was chosen to provide an altitude resolution $s = c\tau/2$ of 50 m, requiring a pulse width $\tau \approx 0.35\ \mu s$. This in turn gives $N' = v\tau/d' + 1 \approx 77$ for the number of elements simultaneously excited. To improve the S/N ratio, 100 pulses are integrated. Because of the 50-kHz prf, a target moving at the moderately high speed (for this application) of 20 m/sec will have changed position by 0.04 m over the 100-pulse presumming interval. Finally, the wavelength is chosen to be $\lambda = 1$ m and the radar cross section to be 0 dBsm (1 m^2).

With the noise bandwidth B set equal to $1/\tau$, the S/N ratio was evaluated as a function of Y for several values of P_o. The P_D was obtained from Figure 11 and the results plotted in Figure 12.

Inspection of the curves show that a peak input power of about 10 W will provide a probability of detection of about 0.9 along the entire length of the

8. Skolnik, M.I. (Ed.) (1970) Radar Handbook, McGraw-Hill, N.Y.

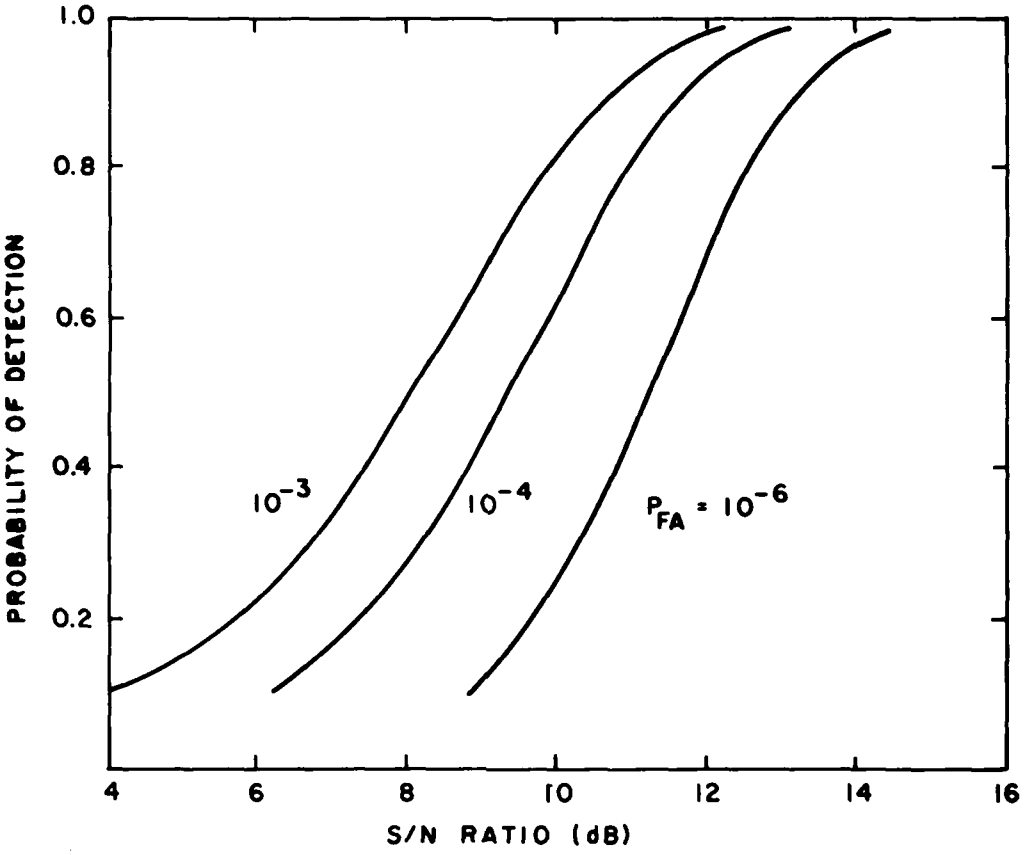

Figure 11. Probability of Detection as a Function of Signal-to-Noise Ratio for a Nonfluctuating Target. Data for curves obtained from Reference 8

sensor to an altitude of 1 km. The short interval of reduced performance at about 250 m (for P_o = 1 W) is a result of the varying near-field gain as a function of altitude. Over this narrow interval, the decrease in S/N produced by the $1/R^4$ loss is greater than the increase in the square of the near-field gain. The rate of increase in the gain decreases with altitude until it reaches the far-field limit of Eq. (31b).

3.4 Measurement of Range and Altitude

When the system is configured in the monostatic mode as shown in Figure 13(a), only the elapsed time between the transmission of a pulse and the reception of its echo can be measured. From the sketch, it is clear that the elapsed time Δt is related to the target location by

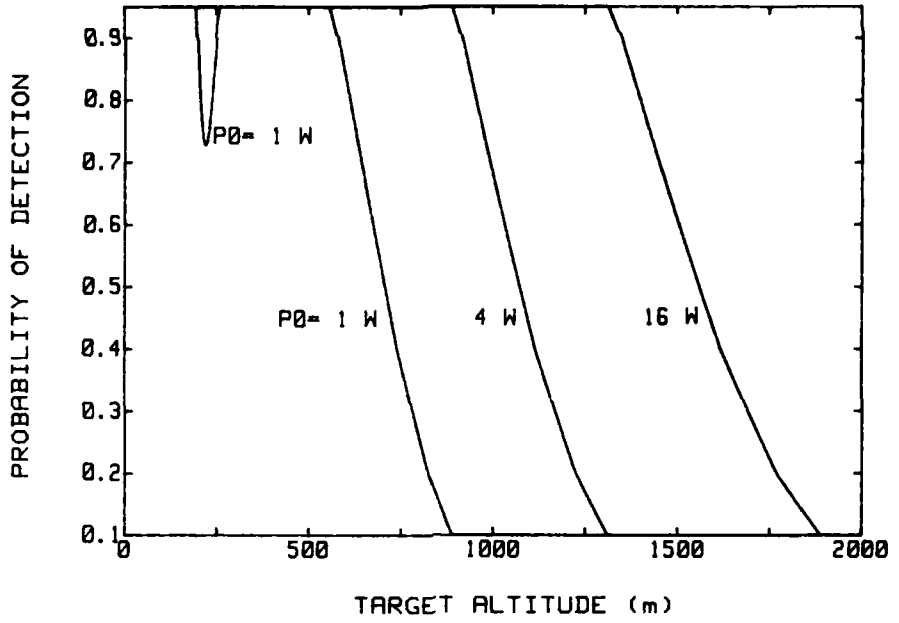

Figure 12. Probability of Detection for a Target at Various Altitudes. α = 0.0025 Neper/m, x_1' = 0 m, $K_1K_1^*$ = -45 dB, σ = 0 dBsm, τ = 0.35 μsec, and λ = 1 m

$$\Delta t = 2(Xd'/vd + Y/c) \tag{33}$$

and that the target can be anywhere along the straight line described by $Y = cXd'/vd + c\Delta t/2$. Thus, the measurement cannot distinguish between range and altitude and only the total range-altitude delay can be measured.

To overcome this problem, the system can be configured into the bistatic mode as shown in Figure 12(b). Here another receiver Rx 2 has been added to measure the difference $\Delta t'$ between the transit time Ld'/vd of the pulse directly to Rx 2 and the propagation time of the pulse down the line to the target, up to the target, and back down to the line to Rx 2. The propagation time for this is $Xd'/vd + 2Y/c + (L - X)d'/vd$. Thus $\Delta t'$ is

$$\Delta t' = 2Y/c \quad , \tag{34}$$

and gives for the target altitude

$$Y = c\Delta t'/2 \quad . \tag{35}$$

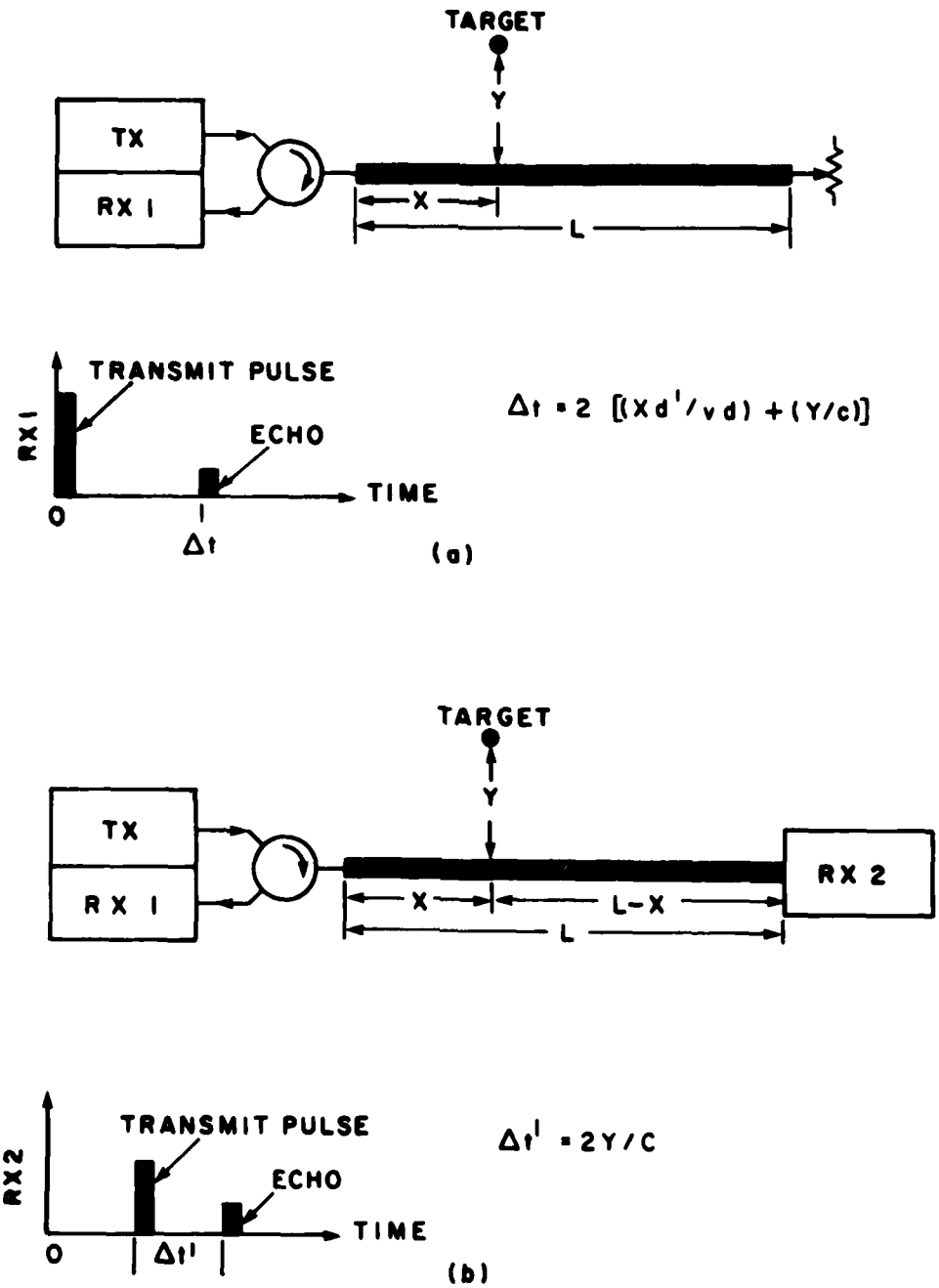

Figure 13. Sketch of System Implementations: (a) Monostatic and (b) Multistatic

From Eq. (33) the range is found to be

$$X = vd(\Delta t - \Delta t')/2d' \quad . \tag{36}$$

The addition of the second receiver allows the unambiguous measurement of both the target's range and its altitude.

It is interesting to use Eq. (33) and the curve in Figure 9(a) to compute the target range X. From Figure 9(a), the time between T and the arrival of the pulse at P(X, Y) is about 792.5 d'/v. To this must be added that portion of T that accounts for the propagation time of the contribution from r_{16}, which is $t_{16} = \{Y^2 + [X - (N' - 1)d/2]^2\}^{1/2}/c$. Thus Δt is twice the sum of 792.5 and t_{16}. Taking $Y = 2(N' - 1)^2 d^2/\lambda$ there results $X = vd[(\Delta t/2) - (Y/c)]/d' = 499.9 \approx 500$ m, the known range of the target.

3.5 Pulse Shaping for Lower Sidelobes

All patterns shown thus far were calculated assuming that the excitation for each element was the same. Such uniform arrays produce the maximum gain obtainable for a given number of elements and exhibit a relatively high sidelobe level. Figures 4 and 5 show that the peak of the first sidelobe is about 13 dB below the peak of the main beam. The sidelobe structure of an array is greatly affected by the relative excitation levels of its elements. The average sidelobe level as well as the distribution of the levels of the sidelobes can be controlled by choosing the appropriate excitation distribution (taper) of the array. Commonly used distributions are the Taylor and Chebyshev tapers. The former produces a pattern that reduces the first n sidelobes to a uniform level and then allows the remainder to fall off gradually. The latter produces a sidelobe distribution with all sidelobes at the same reduced level.

In conventional arrays, the excitation of the elements is controlled by the construction of the beam former, which is designed to produce the desired taper. In the present case, however, the excitation levels cannot be incorporated into the construction of the array because the subarray is formed by the pulse as it moves down the line. Thus it is necessary to control the shape of the pulse by suitably modulating its amplitude. To demonstrate the principle, a simple linear modulation that produces a triangular pulse on a pedestal is used instead of the more complicated Taylor or Chebyshev tapers. The time modulation will result in an element excitation distribution that can be represented by the expression

$$v_m = 1 - \frac{|M+1-2m|(1-\mu)}{M-1} \quad , \quad m = 1 \text{ to } M \text{ (M odd)} \tag{37}$$

and

$$v_m = V_{M+1-n} = 1 - \frac{(M-2m)(1-\mu)}{M} \quad , \quad m = 1 \text{ to } M/2 \text{ (M even)} \quad , \tag{38}$$

where μ is the fractional height of the pedestal.

The effect of modulating the excitation pulse can be computed with Eq. (25) if a factor v_m is inserted to control the amplitudes of the element contributions for which $f[t - (x_n'/v) - (r_n/c)] = 1$. With this change Eq. (25) becomes

$$\bar{E}_\theta = V_o K_1 e^{[-(\alpha+j\beta)x_1' - j\omega t]} \sum_{n=1}^{N} v_m f\left(t - \frac{x_n'}{v} - \frac{r_n}{c}\right) e^{j\beta d'(n-1) + jkr_n\left(\frac{\hat{\theta}}{r_n}\right)} \quad , \tag{39}$$

where $1 \leq m \leq M$ with M determined from Eq. (27) or Eq. (28). $m = 1$ is made to correspond to the first element for which $f[t - (x_n'/v) - (r_n/c)] \geq 0$. The patterns that result when v_m from Eqs. (37) or (38) is substituted into Eq. (39) are shown in Figure 14 for three values of pedestal height. It is apparent that the patterns in Figures 14(a) and 14(b) exhibit a lower sidelobe level and broader beamwidth than does that of the uniform array in Figure 9(a).

The principal benefit of lower sidelobes in radar is to reduce the possibility of interfering signals entering the radar receiver.

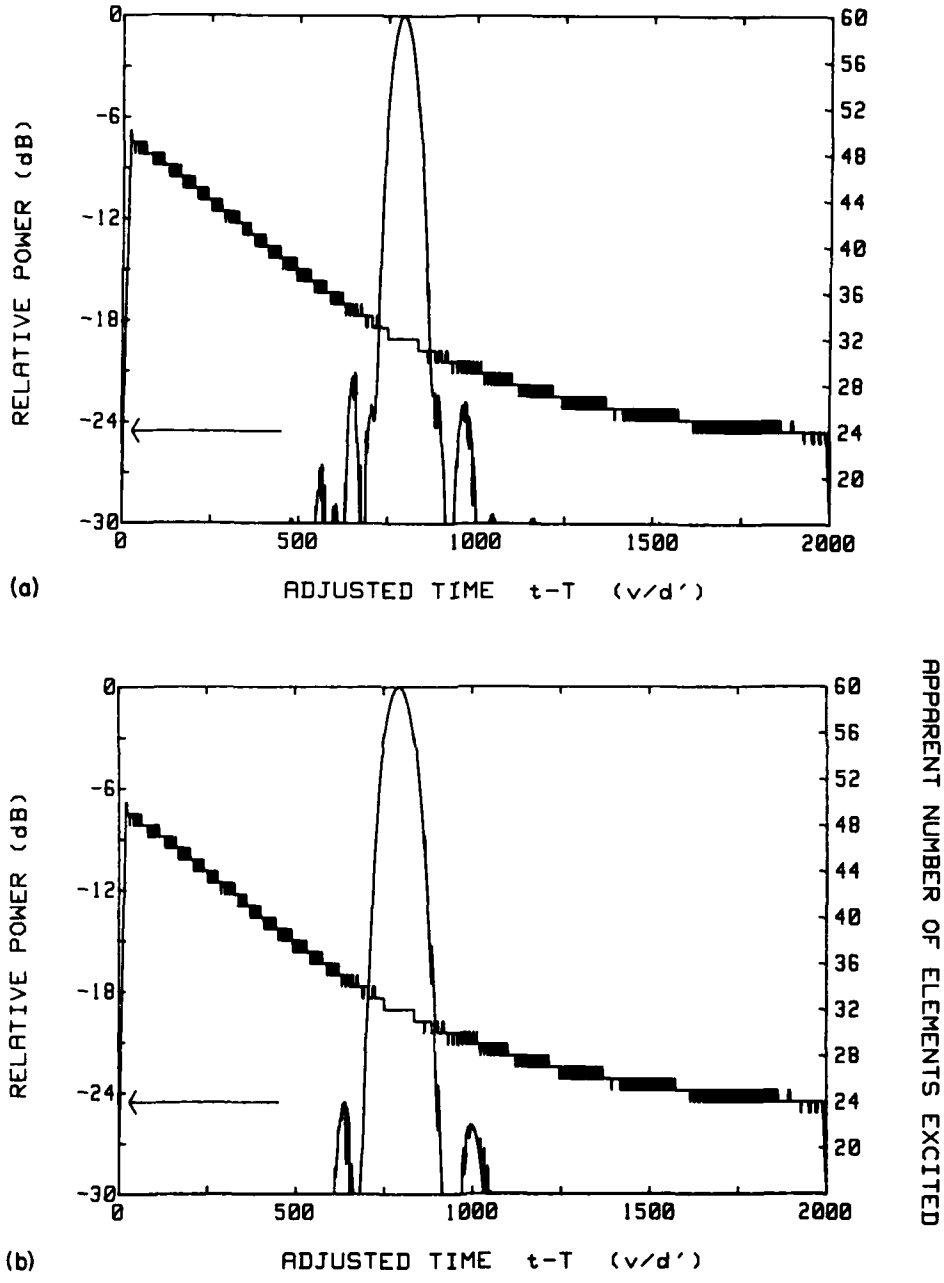

Figure 14. Far-Field Radiation Patterns for a Shaped Pulse System. $L = 1000$ m, $\lambda = 1$ m, $v = 0.73c$, $d' = 0.73$ m, $d = \lambda/2$, $Y = 2(n-1)^2 d^2/\lambda$, $x_1' = 0$, $N' = 32$, $X = L/2$, and $T = [x_1' + (N'-1)d'/2]/v + [Y^2 + (X - (N'-1)d/2)^2]^{1/2}/c$. (a) $\mu = 0.3$, (b) $\mu = 0$

4. CONCLUDING REMARKS

A continuous array of radiators appropriately coupled to a transmission line is proposed for a look-up sensor to detect low-altitude airborne intruders. The chief advantage of such a system is that it produces a continuous vertical zone of protection that extends all the way to the ground with no dead zones or shadows and that follows the perimeter of the installation. To achieve this complete coverage zone however, the physical sensor must also encircle the entire installation.

The use of horizontal dipoles produces maximum gain in the vertical direction. The detection performance decreases gradually [Eq. (1)] away from vertical going to zero toward the horizon(s) away from the longitudinal vertical plane. For the present case, the detection performance is symmetrical about the longitudinal vertical. In certain applications, it may be desired to decrease the detection sensitivity toward the inside of the installation and to increase the sensitivity toward the outside. In such cases, radiators with appropriately shaped element patterns chosen to achieve the proper coverage could be used. In fact, the element patterns of the radiators could be varied along the sensor to shape the coverage as needed.

The maximum length of the sensor is primarily limited by the attenuation of the feeding network. To extend its length, line amplifiers could be used to raise the signal level in the feed transmission line. The coupling coefficients of the sensors must be decreased to offset the gain of the amplifier in order to maintain a uniform detection zone. Also, the allowable pulse repetition frequency will be affected by the length of the sensor.

References

1. GUIDAR Technical Brochure (1980) Computing Devices Co., Ottawa, Ontario, Canada.
2. SPIR Technical Brochure (1980) Computing Devices Co., Ottawa, Ontario, Canada, December 1980.
3. Poirier, J. L. (1980) Estimation of the Zone of Detection of the Single Wire Individual Resource Protection Sensor, RADC-TR-80-258, AD A094137.
4. Gehman, J. B. (1981) Area Intruder Track Study, RADC-TR-81-314, AD A110621.
5. Jasik, H. (Ed.) (1961) Antenna Engineering Handbook, McGraw-Hill, N.Y.
6. Krauss, J. D. (1950) Antennas, McGraw-Hill, N.Y.
7. Skolnik, M. I. (1962) Introduction to Radar Systems, McGraw-Hill, N.Y.
8. Skolnik, M. I. (Ed.) (1970) Radar Handbook, McGraw-Hill, N.Y.

MISSION
of
Rome Air Development Center

RADC plans and executes research, development, test and selected acquisition programs in support of Command, Control Communications and Intelligence (C^3I) activities. Technical and engineering support within areas of technical competence is provided to ESD Program Offices (POs) and other ESD elements. The principal technical mission areas are communications, electromagnetic guidance and control, surveillance of ground and aerospace objects, intelligence data collection and handling, information system technology, ionospheric propagation, solid state sciences, microwave physics and electronic reliability, maintainability and compatibility.

Printed by
United States Air Force
Hanscom AFB, Mass. 01731

END

FILMED

12-84

DTIC